ACTUATORS

Elastomeric passive transmission for autonomous force-velocity adaptation applied to 3D-printed prosthetics

Kevin W. O'Brien[1], Artemis Xu[1], David J. Levine[1]*, Cameron A. Aubin[1], Ho-Jung Yang[2], Michael F. Xiao[2], Lennard W. Wiesner[3], Robert F. Shepherd[1,4†]

The force, speed, dexterity, and compact size required of prosthetic hands present extreme design challenges for engineers. Current prosthetics rely on high-quality motors to achieve adequate precision, force, and speed in a small enough form factor with the trade-off of high cost. We present a simple, compact, and cost-effective continuously variable transmission produced via projection stereolithography. Our transmission, which we call an elastomeric passive transmission (EPT), is a polyurethane composite cylinder that autonomously adjusts its radius based on the tension in a wire spooled around it. We integrated six of these EPTs into a three-dimensionally printed soft prosthetic hand with six active degrees of freedom. Our EPTs provided the prosthetic hand with about three times increase in grip force without compromising flexion speed. This increased performance leads to finger closing speeds of ~0.5 seconds (average radial velocity, ~180 degrees second^{-1}) and maximum fingertip forces of ~32 newtons per finger.

INTRODUCTION

The grip strength, grasping speed, and active degrees of freedom (DOFs) of even the most advanced prosthetic hands pale in comparison with those of a human hand. Developing prosthetic limbs requires designers to make difficult trade-offs among size, weight, force, speed, and cost of the actuation system (*1*). User studies have shown that 90% of patients with myoelectric prostheses consider their prosthetic hand to be too slow and 79% consider it to be too heavy (*2*). On the basis of this user feedback, it is easy to see why state-of-the-art prosthetic hands, such as the BeBionic Hand (Ottobock; ~$11,000) and the iLimb (Touch Bionics Inc.; ~$18,000), rely on high-quality motors such as the Faulhaber 1024SR (~$200) to achieve the necessary precision, torque, and speed in a small enough form factor (*3*). Lower-performing motors of similar size (e.g., Pololu micrometal gearmotors) (*4*, *5*) are substantially lower in cost (~$15) but require choosing between applying sufficient force or speed to the prosthetic. Examples of prosthetic hands that use low-cost motors are Brunel Hand (~$1500; Open Bionics Inc.) (*6*) and open-source initiatives (~$200) from OPENBIONICS (*7*–*9*). The combination of speed and strength of these powered hands is limited due to the use of less costly motors, as well as the materials from which they are made [i.e., acrylic, thermoplastic urethane (TPU), and polylactic acid (PLA)].

A good solution to this classic engineering contradiction of speed versus force is to dynamically adjust the motor's effective gearing ratio. Many of the systems used to accomplish this dynamic adjustment—such as passively variable transmission (*10*), load-sensitive continuously variable transmission (CVT) (*11*), and adjustable power-transmitting mechanism (*12*)—use jointed mechanisms. Another system, demonstrated by Belter and Dollar (*13*), used a variable pitch roller to adjust the angle at which a string spools around a cylindrical rod. Work from Shin *et al.* (*14*) used dual-mode twisting of strings to provide high speed in one configuration and high force in the other. Matsushita *et al.* (*15*) developed a drum CVT that changed the radius at which a string spooled around a cylinder by compressing a spring in the center of the transmission. Felton *et al.* (*16*) demonstrated an origami-inspired CVT wheel, whose dodecahedral fold pattern allowed for the radial compression of reinforced faces to modulate transmission ratio. Although these systems have their merits, they are limited by size, complexity, fabrication techniques, and material requirements. These same requirements preclude three-dimensionally (3D) printing them for compact and custom prosthetics.

Here, we report a simple, low-cost, 3D-printed CVT system that uses elastomeric material. These elastomeric passive transmissions (EPTs) are, essentially, rubber wheels mounted on a rotary motor that spool a wire—they continuously decrease their moment arm as additional load is applied. At no load, they have a large radius and spool quickly for fast actuation but apply less total force because the moment arm is larger. At high load, their radius is passively minimized, so they spool more slowly and apply higher forces (Fig. 1A). EPTs, as spring-like components between the motor and actuator (finger), act as series elastic elements that have been shown to assist in shock tolerance, to improve force control, and to reduce reflected inertia (*17*, *18*).

Many prosthetic hands and robotic grippers have been designed by using tendon-driven actuators (*19*–*30*). To demonstrate the capabilities of our EPTs, we used them to fabricate a six-DOF tendon-driven prosthetic hand that displays an advantageous combination of gripping speed and strength at a low cost. We used a projection stereolithography (SLA) 3D printer to rapidly fabricate customized EPTs and fingers with high resolution. The motor-integrated hand, called ADEPT (adaptively driven via elastomeric passive transmissions), has a mass of ~399 g and a material cost of less than $500.

RESULTS

EPT design

The EPT is an intelligent composite that autonomously adjusts its spooling radius for mechanical advantage based on environmental interaction. We tuned the degree of passive adjustment through the geometry of the EPT. Each EPT is a composite consisting of both high- and low-modulus polyurethanes (HPU and LPU, respectively). The HPU (RPU 70, Carbon Inc.) serves as the core of the EPT, ensuring a rigid connection to the motor shaft. This core is surrounded by a ring

[1]Department of Mechanical and Aerospace Engineering, Cornell University, Ithaca, NY 14850, USA. [2]Department of Electrical and Computer Engineering, Cornell University, Ithaca, NY 14850, USA. [3]Department of Chemical Engineering, Cornell University, Ithaca, NY 14850, USA. [4]Department of Materials Science and Engineering, Cornell University, Ithaca, NY 14850, USA.
*Present address: Department of Mechanical Engineering and Applied Mechanics, University of Pennsylvania, Philadelphia, PA 19104, USA.
†Corresponding author. Email: rfs247@cornell.edu

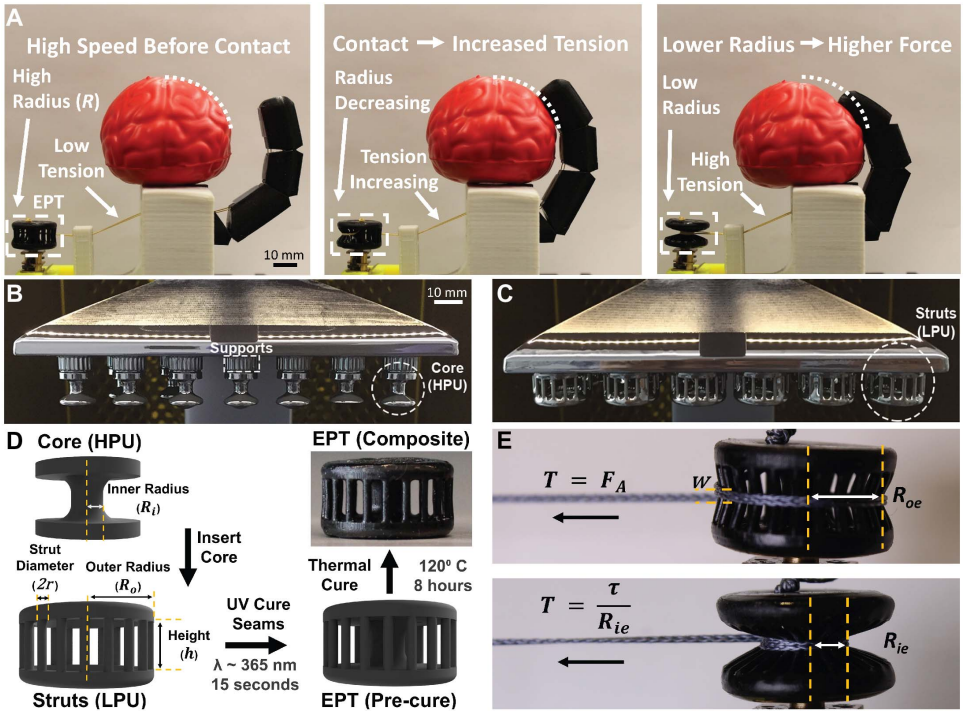

Fig. 1. EPT operation and manufacturing. (**A**) Increasing tendon tension causes a reduction in the spooling radius of the EPT, leading to higher output forces. EPTs are manufactured via projection SLA in two parts: (**B**) a rigid core and (**C**) a ring of elastomeric struts. (**D**) The two parts are cured together to form a polyurethane composite. (**E**) Close-up of the EPTs spooling in high-speed mode (top) and high-force mode (bottom).

of LPU (EPU 40, Carbon Inc.) struts, which give the system its dynamic spooling radius. Our EPTs were printed in two parts and bonded together during the final curing stage (Fig. 1, B to D). We used continuous liquid interface production (CLIP) projection SLA (*31*) to rapidly print and iterate the design of both components of the EPT (movie S1). Three-dimensionally printing the EPTs allowed us to reduce manual effort in fabrication and to enable production of personalized parts less expensively and at a lower volume than alternative manufacturing approaches (*32*).

EPTs can be used with any tendon-driven actuation system by spinning with their motor shaft and winding a tendon around their circumference. Under no tension, the EPT struts are undeformed, and the spooling radius is large for high-speed actuation. As the tension increases, the struts are pulled into the center, and the spooling radius decreases passively until an equilibrium between the tendon force and stress in the struts is reached. The spooling radius is minimized, and tension is maximized, when the motor reaches its stall torque (τ). The change in spooling radius due to tension, $R_T = R_o - R$, can be solved for using Eq. 1

$$T\cos\left(90° - \frac{180°}{N}\right) = E\pi r^2 \frac{\left(\sqrt{R_T^2 + \left(\frac{h}{2}\right)^2} - \frac{h}{2}\right)}{\frac{h}{2}} \cos\left(\operatorname{atan}\left(\frac{\frac{h}{2}}{R_T}\right)\right) \quad (1)$$

where R_o is the outer radius and R is the current radius. After the LPU struts contact the HPU inner core, they are compressed, resulting in further reduction of radius modeled by Eq. 2

$$R_C = R_i + 2re^{\frac{T_c - T}{R_i E_c w}} \quad (2)$$

In these equations, h is the height of the elastomeric struts, N is the number of struts, R_i is the radius of the inner core, r is the radius of the struts, and w is the width of tendon contact with the EPT; these geometric parameters can be seen in Fig. 1. T_c is the tension at which the struts initially contact the core of the EPT, E is the storage modulus of LPU in tension, and E_c is the compressive modulus (fig. S1). Because of nonlinearities in these properties, we approximated E and E_c each as five-part piecewise functions. The calculated results were smoothed with a moving average to simulate by using continuous E and E_c. In our model, we defined the spooling radius, R, as $R = R_o - R_T$ before the struts come in contact with the rigid core (for $R > R_i + 2r$) and $R = R_C$ after the struts contact the rigid core (for $R < R_i + 2r$).

To assess and compare different EPT designs, we defined two geometric and material property–dependent characteristics for the EPTs: (i) SRR_{max}, the maximum spooling radius ratio (SRR), and (ii) SRR_{eff}, the effective SRR in operation with a motor and an actuator. The SRR can be viewed as the amount by which an EPT will multiply the stall force of a tendon-driven actuator as compared with a rigid spool of the same outer radius. SRR_{max} is only dependent on the geometry of the EPT and is defined simply by $SRR_{max} = R_o/(R_i + r)$. SRR_{eff}, on the other hand, incorporates the material properties; the initial change in radius due to the mechanical resistance of the unloaded actuator, F_A; and the maximum change in radius based on the stall torque (τ) of the motor. We define the effective SRR as

$$SRR_{eff} = R_{oe}/R_{ie}$$

where the effective outer radius, R_{oe}, is the spooling radius when an unloaded actuator is fully actuated (when $T = F_A$), and R_{ie} is the spooling radius when the motor stalls and can be solved for by using Eqs. 1 or 2

with $T = \frac{\tau}{R}$ (Fig. 1E). Ideally, the EPT is stiff enough to resist changes in radius when driving an unloaded actuator and soft enough to allow the motor to cause a large change in radius before stalling.

To evaluate the validity of our mathematical model, we fabricated EPTs with varying SRR_{eff} values for experimental testing and named them according to Fig. 2A. For example, EPT 2 has $N = 20$ struts, $r = 0.625$ mm, $h = 7$ mm, and $R_o = 10$ mm. All the EPTs we tested had an $R_i = 2.5$ mm, due to the size of the motor shaft. We compared experimental spooling radius versus tendon tension with the theoretical model (Fig. 2B).

Parametric model

To better understand how changes in geometry affect the performance of our EPTs, we created a parametric model using Eqs. 1 and 2. We simulated various EPT geometries by varying parameters N, h, r, and R_o and holding $R_i = 2.5$ mm, $\tau = 0.19$ Nm, $F_A = 2.5$ N, and the LPU material properties constant. We evaluated how changes in these parameters affect SRR_{eff}, strut tensile strain (Fig. 3), and stress (fig. S2). We were interested in the strain and stress because of their impact on the fatigue life of the EPTs (further discussed in the EPT fatigue life section). We determined the experimental strut strain, strut stress, SRR_{eff}, R_{ie}, and R_{oe} of each EPT geometry from Fig. 2.

The best EPT for a given F_A and τ would be the one with the highest SRR_{eff} while having the lowest strut strain and stress. On the basis of our model, we see that we can increase the stiffness of an EPT by decreasing the height of the struts (h), increasing the number of struts (N), or increasing the strut radius (r); however, changing each of these parameters has inherent limitations. Decreasing the height of the struts increases the strain, thus reducing the fatigue life of the device. Increasing the number of struts causes overcrowding when closer to the inner core (not modeled), thus increasing R_{ie} and reducing SRR_{eff}. Increasing strut radius also increases R_{ie}, again reducing SRR_{eff}. Increasing R_o has the potential to increase SRR_{eff} (given a strong enough motor), but this increases strut strain, unless the increase in R_o is matched with an increase in h. To maintain low strains for fatigue life, the ratio between R_o and h should be kept constant. From the results of this model, we chose to use EPT 2 because it has the highest SRR_{eff} with the proper volume for use in our ADEPT hand.

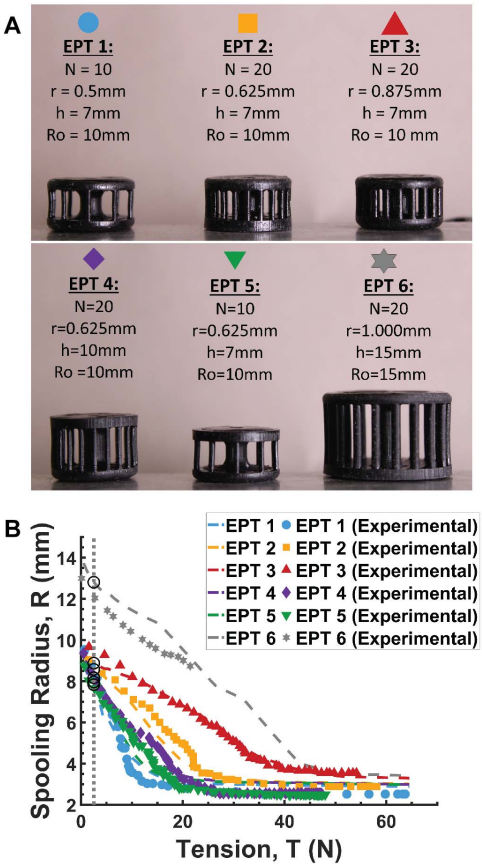

Fig. 2. EPT characterization. (**A**) Six EPTs with different geometries. (**B**) The spooling radius of the six EPTs as a function of tendon tension (solid symbols) compared with their theoretical values (dashed lines).

EPT fatigue life

The benefits of elastomeric transmission systems are that they can be 3D printed quickly (50 per hour), cheaply (<$1 per part), and in many compact form factors. However, the elastomers we presently use to print EPTs are subject to wear from repeated use, leading to failure in the form of LPU strut breakage. Although they remain functional for actuation, the SRR of an EPT decreases with each broken strut. To evaluate the fatigue life of the EPT as a whole, we define failure as a 2.5% drop in SRR_{eff}, which, based on our model, corresponds to four broken struts in the EPTs that we measured for fatigue life.

We conducted a series of cyclic loading tests to quantify and to extend the fatigue life of EPTs. We found that the cycles to failure, C_f, for EPT 2 in high-speed mode ($T \sim F_A + 1$ N) was 2497 ± 1115 (mean ± SD) cycles and that failures occurred at the points of bending in the LPU (fig. S3), not in contact with the tendon. This indicates that failure was not caused by frictional abrasion of the constituent LPU but simply by accumulated plastic deformation due to crack propagation, meaning that the fatigue life can be increased by reducing the strain of and the stress applied to the struts.

When cycled to maximum force (high-force mode), EPT 2 demonstrated a reduced fatigue life of $C_f = 49 \pm 27$ cycles. In high-force mode, the maximum stress encountered by the EPT was $\sigma_{max} \sim \frac{T}{wR} \sim 10$MPa (*33*), corresponding to a strain of $\varepsilon \sim 270\%$ (Fig. 4A). Cyclic testing of LPU samples in tension (Fig. 4B) at $\varepsilon \sim 270\%$ resulted in $C_f = 32 \pm 15$ cycles—verifying the wear mechanisms of the EPT in high-force mode.

With this information, we improved the service life of the EPT by using two mechanical design changes intended to decrease local stresses and strains on the struts. While these stress reductions increase fatigue life, they also decrease SRR_{eff}. The first change, doubling the tendon diameter, caused a drop in $SRR_{eff} = 2.63 \pm 0.07$ while increasing C_f to 2743 ± 146 cycles and 200 ± 32 cycles in high-speed mode and high-force mode, respectively. The second change was to extend the LPU section from the struts toward the core at the top and the bottom of the EPT. We did this to simulate having a taller EPT, because our parametric model shows that increasing the height can lower the strain to increase the fatigue life while maintaining a small form factor. This change, in conjunction with the increased tendon diameter (fig. S4), lowered the SRR_{eff} to 2.18 ± 0.07 and led to a small increase in fatigue life in high-speed mode, $C_f = 3140 \pm 907$ cycles, and a significant increase in high-force mode, $C_f = 458 \pm 167$ cycles. The high-force fatigue life of the EPTs incorporating these changes is consistent with the cyclic performance of LPU in tension at or below $\varepsilon = 175\%$ ($C_f = 274 \pm 40$ cycles).

Although these reductions in stress increased the fatigue life of EPTs, the most drastic improvements were due to the use of a new,

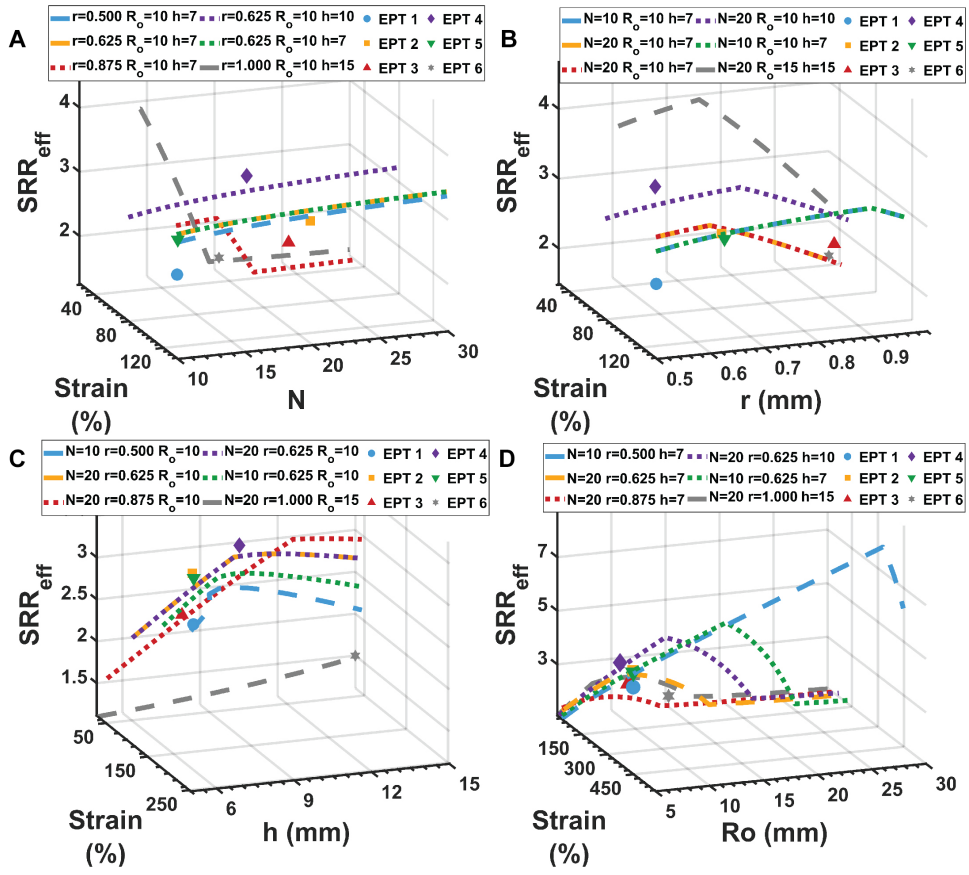

Fig. 3. Parametric model. SRR_{eff} and strut strain when varying (**A**) the number of struts (*N*) from 10 to 30, (**B**) the strut radius (*r*) from 0.5 to 1 mm, (**C**) the height (*h*) from 5 to 15 mm, and (**D**) the outer radius (R_o) from 5 to 30 mm. The dotted lines are the model results with the constant parameters shown in the legend and the symbols representing experimental data for the six EPT geometries.

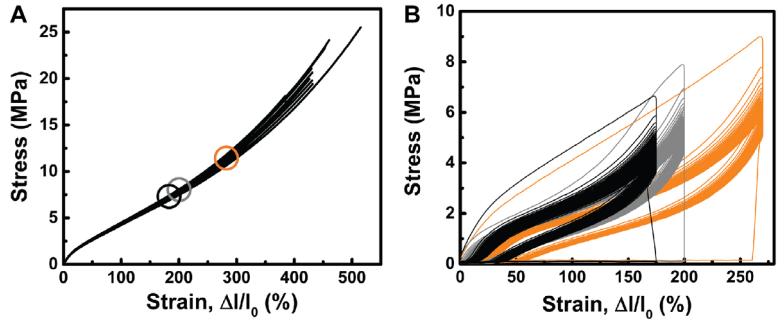

Fig. 4. LPU fatigue life. (**A**) Tensile strain performance, to failure, for seven samples of LPU. (**B**) Cyclic tensile loading and unloading performance of LPU at strains corresponding to the colored circles in (A).

limited-release LPU material (EPU 41, Carbon Inc.). This material, in conjunction with the stress reduction techniques discussed previously, led to a high-speed fatigue life of more than 25,000 cycles (single-strut breakage, 0.3% drop in SRR_{eff}) and a high-force fatigue life of 1991 ± 153 cycles while maintaining a higher SRR_{eff} of 2.5 ± 0.02 due to the increased storage modulus (*34*).

EPT-driven actuator performance

We conducted two sets of experiments to characterize the performance of our EPT in a tendon-driven finger actuator. First, we measured the maximum force that we could apply at the tip of the finger, FF (Fig. 5A). In the second experiment, we measured the closing speed of the fingertip, Γ (Fig. 5B), when its motion was unimpeded. Γ is the average radial velocity about the synthetic metacarpophalangeal joint according to Belter *et al.* (*35*). In each of these experiments, we compared EPT 2 with an array of rigid spools with different radii (Fig. 5C). Our $r = 10$ mm EPT closed the finger in 450 ms ($\Gamma \sim 180° s^{-1}$), the same maximum flexion speed as an $r = 9$ mm rigid spool, and delivered a maximum fingertip force (FF ~ 32 N) equivalent to an $r = 3$ mm rigid one. These results show that our EPT achieved the high-speed benefits

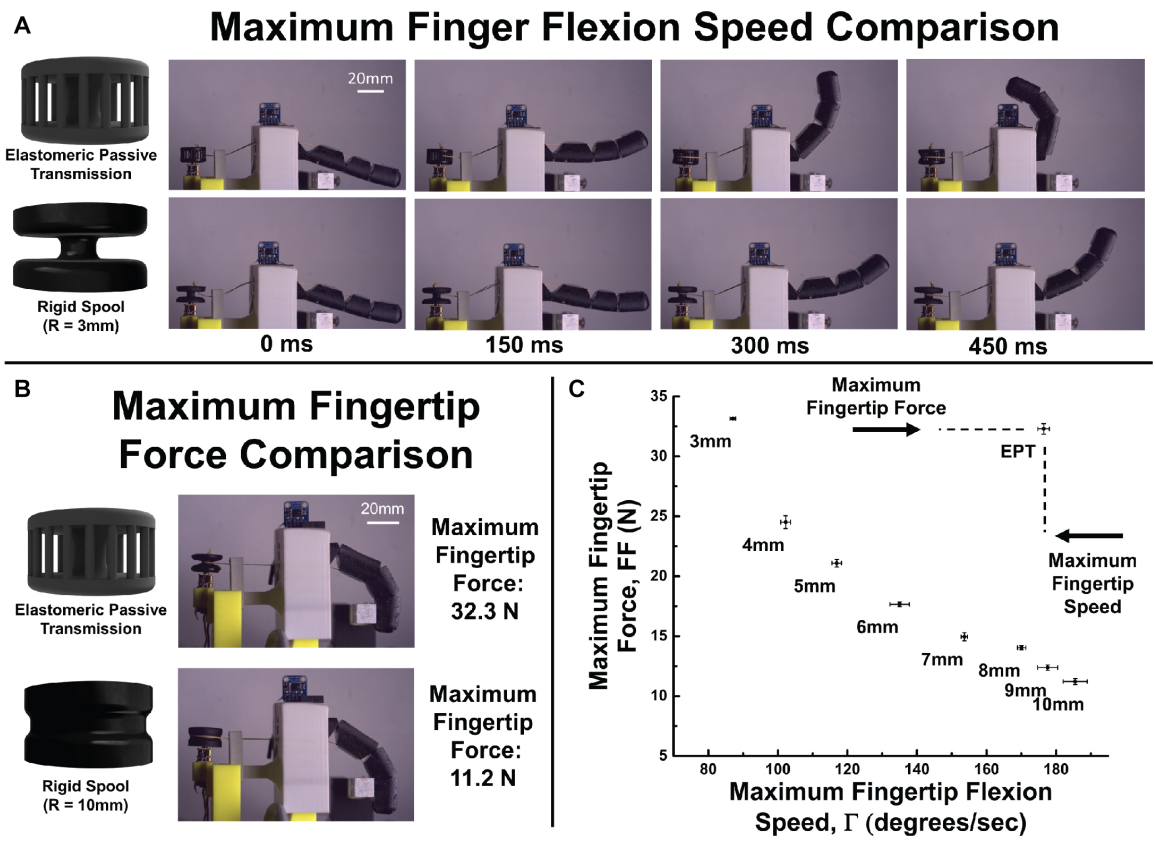

Fig. 5. EPT-driven finger performance. Comparisons of the (**A**) unloaded finger closing time and (**B**) maximum fingertip force between an EPT and rigid spools. (**C**) The EPT performance outside the Pareto Front for speed and force generated by rigid spools of varying radii. Error bars indicate SD.

of a large-radius spool while still delivering the high force of a small-radius one.

Design of the ADEPT hand

The ADEPT hand was composed almost entirely of 3D-printed components (Fig. 6A). Each finger was printed from LPU with three living hinges, a thickness of ~0.5 mm, and three chambers for integrating the extrasensory tactile array (ETA) sensors. The living hinges of the thumb were oriented at 25° from the horizontal plane to promote twisting toward the palm upon actuation (Fig. 6B). The thumb also contained a mesh at its base that allowed us to emulate the movement of a ball joint by using a single elastomeric component. The fingers were driven by inexpensive geared DC motors (~$15; 298:1 Micro Metal Gearmotor HP 6V, Pololu Corporation) with the exception of the thumb, which was driven by two motors—one for each of its two active DOFs. The motors were powered by a two-cell (7.4 V), 500-mAh lithium polymer battery that also resides in the palm of the hand. Although the motors are classified as 6-V motors, it is common practice to drive 6-V motors as high as 9 V for prosthetic applications (*36*).

The palm of the hand consisted of an inner plate and an outer casing (both printed with HPU). The inner plate secured the six motors and associated electronics; the outer casing had an LPU skin on the palm to increase its softness and friction for grasping. With the two-cell battery, the hand had a mass of 399 g (365 g not including the battery)—less than the mass of the average human hand (~400 g).

In addition, we integrated force and proximity sensing into each finger of our ADEPT hand for improved control. ETA sensors, based on work from Patel and Correll (*37*), were composed of flexible printed circuit boards with three infrared proximity sensors covered in a layer of silicone rubber. By changing the type of coating rubber, we could adjust the behavior of a sensor on the ETA. In this work, we demonstrated two types of sensors: (i) proximity and (ii) tactile. The proximity ETA was created by coating the optical sensors with a transparent silicone (Solaris; Smooth-on Inc.) and assisted with controlling the timing of a grasp. The transparent silicone leads to a sensing range (d) of ~80 mm but suffers from poor force tracking under 20 N due to a nonmonotonic relationship between sensor reading and force in this range (figs. S5 and S6). The tactile ETA sensor is coated with a more opaque silicone (EcoFlex 35 FAST, Smooth-On Inc.), which leads to a shorter sensing range (d ~ 16 mm) but improved force tracking. In combination with the series elasticity of the EPT, ADEPT has the capacity for high-fidelity force control, which is more desirable than position control in unstructured environments (*38*). We dropped a 150-g ball onto the tip of a finger actuator (Fig. 7A and movie S2) and used the ETAs to measure the proximity and force of the ball. Figure 7 helps to visualize the seamless transition between the proximity (Fig. 7B) and tactile (Fig. 7C) sensors in the ETA. In this figure, you can see the bouncing ball, including the height of each bounce, the distinct instances of contact, and the force upon contact with the finger. This extrasensory perception allowed our ADEPT hand to catch a thrown ball (further discussed in the next section).

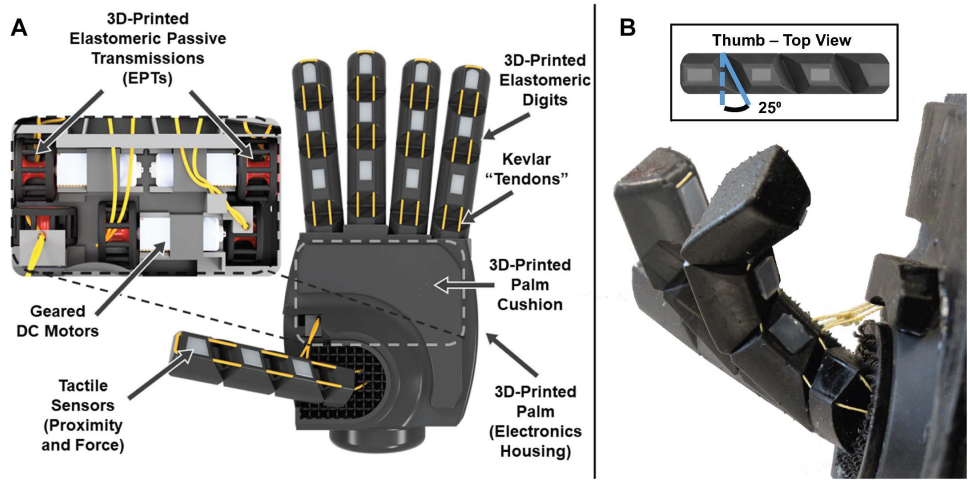

Fig. 6. The ADEPT prosthetic hand. (**A**) A rendering of the ADEPT hand with its main components listed. (**B**) Time-lapse image of thumb flexion demonstrating its angled joints. The 3D-printed fingers are ~85 mm long.

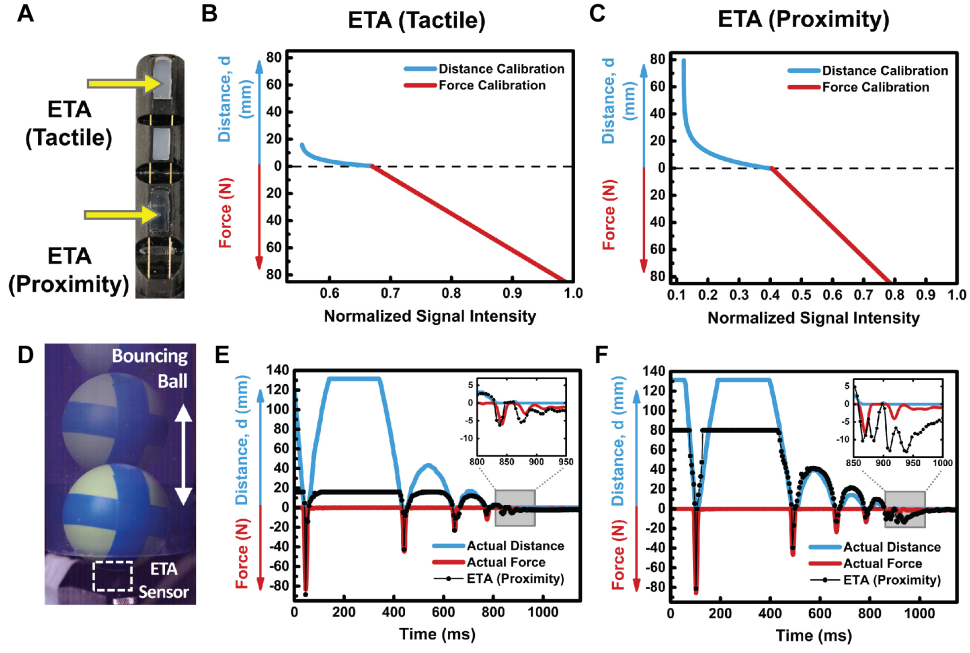

Fig. 7. ETA sensor demonstration. (**A**) Finger actuator with tactile and proximity ETA sensors labeled. (**B**) Calibration curve for the ETA (tactile) sensor; normalized signal intensity is the ratio of the signal reading to the maximum value of the sensor (16-bit unsigned integer). (**C**) Calibration curve for the ETA (proximity) sensor. (**D**) Time lapse depicting the motion of a ball dropped onto ETA sensors to demonstrate force and proximity sensing. (**E**) Results of a single ball drop experiment for an ETA (tactile) sensor. (**F**) Results of a separate ball drop experiment using an ETA (proximity) sensor.

Speed and force demonstrations

With the help of the ETA sensors and the speed afforded by the EPT, the ADEPT hand is capable of catching objects thrown to it (Fig. 8A and movie S3). In these demonstrations, the hand caught and held multiple objects, including a 20-g stress ball and a 12-oz soda can (empty weight, ~13 g). The ETA sensors detected the approaching object at $d \sim 7.5$ cm, which triggered closing of the fingers and thumb around the object. Along with the flexion speed necessary to catch a thrown ball, the ADEPT hand has the strength to crush aluminum cans (Fig. 8B and movie S3) and hold heavy objects such as a wrench (900 g; movie S3). Without the EPT, our tendon-driven hand would have either the speed to catch a ball or the strength to crush a can, but it would not be capable of having both.

DISCUSSION

The EPT allowed us to create actuators with a two- to threefold increase in output force while maintaining maximum flexion speed as compared to a rigid spool with similar radius. The simplicity of our EPT allows it to be small, lightweight, and inexpensive to manufacture with limited manual effort and also allows us to quickly adjust the size and SRR_{eff} of each device to work with a variety of different motors. Although

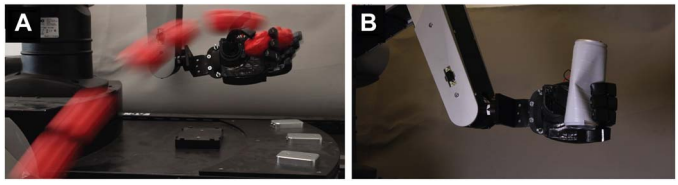

Fig. 8. Speed and force demonstration. (**A**) Time-lapse image of the ADEPT hand catching a thrown ball. ETA sensors detected the ball approaching at ~7.5 cm and triggered closing of the hand. (**B**) Demonstration of the ADEPT hand crushing an aluminum can.

we have focused on SRR_{eff} and fatigue life as the metrics of interest in the evaluation of our EPTs, it is important to note that efficiency is another key metric that is outside the scope of this work.

On the basis of our cyclic experiments, we determined that EPT failure is caused by crack propagation (*39*) in the LPU struts due to cyclic loading. One short-term solution to this issue is to simulate muscle fatigue by limiting the number of high-force cycles that the hand can perform in a day (*40*). Another approach is improving the mechanical design to reduce stress concentration for improved resilience. The root cause for cyclic failure of the EPTs is attributed to the low fatigue life of current SLA 3D-printed elastomers. As the material library for SLA printable elastomers grows (*41*, *42*), using material with improved fatigue properties may increase fatigue life as exhibited when using EPU 41.

We used our inexpensive EPTs to solve a persistent engineering contradiction in powered prosthetic hands—simultaneous high-speed (180° s^{-1}) and high-force (32 N) precision grasping, similar to the abilities of a human hand performing daily activities (200° s^{-1}, 96 N) (*36*). Because of the compact form of the transmission system and the design freedom of SLA 3D printing, we were able to co-design the batteries, motors, and tendons to be contained within the form of the hand while weighing less than 400 g. In comparison, the BeBionic prosthetic, as one example, locates the batteries outside of the hand and weighs ~500 g (*36*). By incorporating EPTs into our 3D-printed ADEPT prosthetic hand, we have demonstrated one of many promising use cases for our passively adaptive transmission system. We believe that these benefits could also expand the capabilities of actuators in other areas, such as active tendons (*43*), soft exosuits (*44*–*47*), and bioinspired mobile robots (*48*–*50*).

MATERIALS AND METHODS

Fabrication of EPTs

We generated the computer-aided design (CAD) files for our EPTs by using Fusion 360 (Autodesk Inc). We printed the HPU cores and LPU struts separately by using projection SLA (M1, Carbon Inc.). After cleaning the two parts, we inserted the HPU cores into the LPU struts and coated the seams with a thin layer (~0.5 mm) of liquid LPU resin, and the assembled structures were cured for 15 s with ultraviolet (UV) light (365 nm; ECE 5000 Flood, DYMAX Inc.). After UV curing, the EPTs were thermally cured at 120°C for 8 hours to produce an HPU/LPU composite.

Fabrication of the ADEPT hand

To fabricate the ADEPT hand, we designed the components with Fusion 360 and printed them with projection SLA. The motors were secured inside the palm with compression-fitting straps (LPU). Each motor was driven by a DC motor driver breakout board (BD65496MUV, Pololu Corporation). The current draw of each motor was measured with high-side current sensor breakout boards (INA 219 High Side DC Current Sensor Breakout Board, Adafruit Industries LLC). These motor drivers and current sensors were controlled by a microcontroller breakout board (Feather 32u4 Bluefruit LE, Adafruit Industries Inc.). The microcontroller, motor drivers, and current sensors were powered by a one-cell (3.7 V) LiPo battery (LP402025, PKCELL Battery Co.), while the motors were powered by a separate two-cell (7.4 V) LiPo (2S20C-500, DLG Electronics Technology Co.). After soldering and securing the electronics to a custom-designed and printed plate in the palm (HPU), we slid the EPTs onto the motor shafts and the fingers and thumb into their respective recesses. In the next step, we threaded the Kevlar threads (KEV138NATL01B, Weaverville Thread Inc.) through channels in the fingers and palm and tied them off at their EPT (one tendon thread per EPT). Finally, we screwed the front and the back casings to the plate of the palm. The back casing was printed with HPU, and the front casing was composed of HPU cured to an LPU lattice and membrane to promote friction and grasping.

Table 1. Piecewise tensile storage modulus used in the model for each strain range.

Strain range	$\varepsilon \leq 10\%$	$10\% \leq \varepsilon \leq 18\%$	$18\% \leq \varepsilon < 25\%$	$25\% \leq \varepsilon < 50\%$	$50\% \leq \varepsilon$
E (MPa)	10.6	7.33	4.88	4.77	3.00

Spooling radius–versus–tension and spooling radius ratio experiments

To measure the relationship between tendon tension and spooling radius, we connected the EPTs to a 298:1 gear motor (Micro Metal Gearmotor HP 6V, Pololu Corporation). For each measurement, we tied a tendon between the EPT (the tendon was wound once around the EPT without deforming the EPT struts) and a push/pull force gauge (Torbal FC200, 200 ± 0.05 N). We ran the motors at 7.5 V and captured images of the deformed EPTs at stall (maximum torque). We analyzed each of the images by using ImageJ to determine the spooling radius of the EPT. We conducted seven trials for each of the EPT and motor combinations and averaged the data to generate the data points in Fig. 2B. The SD for spooling radius did not exceed 0.1 mm for any of these data points. The SD of the measured force did not exceed 0.5 N except for the highest force data points for EPT 1 (SD = 1.68 N) and EPT 2 (SD = 3.22 N).

The data from the spooling radius–versus–tension experiments when the motor stalled were used for the effective inner radius (R_{ie}) in our effective SRR (SRR_{eff}) measurements (Fig. 2B). The effective outer radius (R_{oe}) was determined by driving a finger actuator with our 298:1 gear ratio motor and each of our three EPT geometries. We captured images of the EPT deformation when the unloaded finger was fully actuated and used ImageJ to determine the effective spooling radius. The reported values for SRR_{eff} were generated by dividing the averaged data for R_{oe} over seven trials by the averaged data for R_{ie} over seven trials.

Modeling of spooling radius versus tension

When $R > R_i + 2r$, we calculated with Matlab the tension required to get to the end of the strain range using a specific storage modulus seen in Table 1. If that tension was higher than the tension $\left(T = \frac{\tau}{R}\right)$ provided by a stalled motor at that radius, then we solved for R_t with Eq. 1 using that *E*. Otherwise, we added that tension to Eq. 1 and repeated with the next strain range and *E* until *R* at stall was found. If the model began compression ($R < R_i + 2r$) but did not stall, using the piecewise E_c found in

Table 2. Piecewise compressive modulus used in the model for each strain range.

Strain range	$\varepsilon <$ 4%	4% $\leq \varepsilon <$ 6%	6% $\leq \varepsilon <$ 10%	10% $\leq \varepsilon <$ 50%	50% $\leq \varepsilon$
E_c (MPa)	0.030	1.91	3.90	15.1	30.0

Table 2, we set T_c equal to the tension required to get to the start point (either the beginning of compression for the first E_c or the tension required to get to the next strain range for the following E_c) and $2r$ to be the R at the start of the strain range with R_i subtracted. Just like the tensile section, the limits were tested and equations were solved until stall torque was reached.

Fatigue testing of EPTs

The fatigue life of EPTs was tested while driving a finger actuator. Each represented fatigue life data point included $n = 3$ EPT specimens. The number of cycles was counted until the fourth LPU strut was broken. Tensile testing of LPU was conducted with a Zwick/Roell tensile testing machine. Fatigue life data of LPU consist of $n = 3$ data points with the exception of cyclic testing at $\sigma = 80\%$, which includes only $n = 2$ data points. There are only $n = 1$ EPU 41 high-speed and $n = 3$ high-force tests.

Force characterization of EPT-driven finger actuators

To gather maximum fingertip force data for our finger actuators, we applied 7.5 V to the motor (298:1 Micro Metal Gearmotor HP 6V, Pololu Corporation) driving the actuator using a DC power supply (1745A, B&K Precision Corporation) until the motor stalled. While the motor was running, we measured the fingertip force with a 5-kg loadcell (Load Cell Sensor 0-5 kg, UXCELL). The loadcell output was amplified by using an amplifier breakout board (Sparkfun Loadcell Amplifier—HX711, Sparkfun Electronics Inc.). The amplified signals were read with an Arduino Uno (Arduino AG). The highest force value for each experiment was recorded. The reported maximum fingertip force values are the average of 10 experiments.

Speed characterization of EPT-driven finger actuators

To measure the flexion speed of our EPT-driven fingers, we mounted them to a 3D-printed testing rig with an attached infrared proximity sensor (VCNL 4010, Vishay Intertechnology Inc.). A command from the user to actuate the finger also started a timer within the microcontroller. We determined a threshold value of the infrared sensor that was associated with full flexion of the finger. When this threshold value was exceeded, the microcontroller stopped the timer. We captured images (EOS REBEL T3i, Canon U.S.A. Inc.) of the finger in the unactuated state and used ImageJ to measure the angle between each of the joints in the finger. The reported flexion speed is the number of degrees traversed by the metacarpophalangeal (MCP) joint (determined via ImageJ) divided by the closing time reported by the microcontroller. The reported maximum finger flexion speeds are the average of 10 experiments.

ETA sensor demonstrations

We compared the force and proximity readings of our ETA sensors by placing the end of a finger actuator on top of a push/pull force gauge (Torbal FC200, Scientific Industries Inc.) with the ETA sensor facing up. We dropped a 150-g ball (Rubber Lacrosse Ball, Dick's Sporting Goods Inc.) from a height of 60 cm through a clear acrylic tube and filmed the ball bouncing on the finger with a high-speed camera (Phantom Miro 310, Vision Research Inc.). We analyzed the frames of the resulting videos with ImageJ to determine the height of the ball at each time step.

The ETA sensors were calibrated by using the same method as the ball drop characterization—we held the 150-g ball above the sensor at known heights (using our camera and ImageJ) and pushed the ball against the sensor with known forces (using our push/pull force gauge). We used Origin 2016's (OriginLab Inc.) curve-fitting functions to determine the mapping between raw sensor data and reported measurements (distance and force). We found that the Asymptotic1 Exponential function ($y = a - bc^x$) was best suited for the proximity calibration of our sensors.

SUPPLEMENTARY MATERIALS

robotics.sciencemag.org/cgi/content/full/3/23/eaau5543/DC1
Fig. S1. Uniaxial compressive performance of LPU.
Fig. S2. Two-dimensional parametric model graphs.
Fig. S3. Strut failure due to cyclic bending in the EPT.
Fig. S4. Alternative EPT design.
Fig. S5. ETA (tactile) force tracking.
Fig. S6. ETA (proximity) force tracking.
Movie S1. EPT printing.
Movie S2. Finger sensor–ball drop test.
Movie S3. ADEPT hand demos.

REFERENCES AND NOTES

1. J. T. Belter, A. M. Dollar, Performance characteristics of anthropomorphic prosthetic hands. *IEEE Int. Conf. Rehabil. Robot.* **2011**, 5975476 (2011).
2. C. Pylatiuk, S. Schulz, L. Döderlein, Results of an Internet survey of myoelectric prosthetic hand users. *Prosthet. Orthot. Int.* **31**, 362–370 (2007).
3. Innovation goes hand in hand, www.faulhaber.com/en/markets/medical-laboratory-equipment/small-dc-motors-for-myoelectric-prosthesis/.
4. MICROMO Motion System Selector; www.micromo.com/productselector.
5. Pololu - 298:1 Micro Metal Gearmotor HPCB 6V; www.pololu.com/product/3069.
6. World first for 3D printing and bionics, www.openbionics.com/blog/world-first-for-3d-printing-and-bionics [accessed 25 June 2017].
7. A. G. Zisimatos, M. V. Liarokapis, C. I. Mavrogiannis, K. J. Kyriakopoulos, Open-source, affordable, modular, light-weight, underactuated robot hands, in *2014 IEEE/RSJ International Conference on Intelligent Robots and Systems (IROS 2014)* (IEEE, 2014), pp. 3207–3212.
8. M. V. Liarokapis, A. G. Zisimatos, M. N. Bousiou, K. J. Kyriakopoulos, Open-source, low-cost, compliant, modular, underactuated fingers: Towards affordable prostheses for partial hand amputations, in *2014 36th Annual International Conference of the IEEE, Engineering in Medicine and Biology Society (EMBC 2014)* (IEEE, 2014), pp. 2541–2544.
9. M. V. Liarokapis, A. G. Zisimatos, C. I. Mavrogiannis, K. J. Kyriakopoulos. OPENBIONICS: An open-source initiative for the creation of affordable, modular, light-weight, underactuated robot hands and prosthetic devices, in *2nd ASU Rehabilitation Robotics Workshop* (Arizona State University, 2014).
10. J. Ingvast, J. Wikander, C. Ridderström, The PVT, an elastic conservative transmission. *Int. J. Rob. Res.* **25**, 1013–1032 (2016).
11. T. Takaki, T. Omata, Load-sensitive continuously variable transmission for robot hands. *J. Rob. Soc. Japan* **23**, 238–244 (2005).
12. Y. Ishikawa, W. Yu, H. Yokoi, Y. Kakazu, Development of robot hands with an adjustable power transmitting mechanism, in *Intelligent Engineering Systems Through Neural Networks* (ASME Press, 2000), vol. 10, pp. 631–636.
13. J. T. Belter, A. M. Dollar, A passively adaptive rotary-to-linear continuously variable transmission. *IEEE Trans. Robot.* **30**, 1148–1160 (2014).
14. Y. J. Shin, H. J. Lee, K.-S. Kim, S. Kim, A robot finger design using a dual-mode twisting mechanism to achieve high-speed motion and large grasping force. *IEEE Trans. Robot.* **28**, 1398–1405 (2012).
15. K. Matsushita, S. Shikanai, H. Yokoi, Development of Drum CVT for a wire-driven robot hand, in *2009 IEEE/RSJ International Conference on Intelligent Robots and Systems* (IEEE, 2009), pp. 2251–2256.

16. S. M. Felton, D.-Y. Lee, K.-J. Cho, R. J. Wood, A passive, origami-inspired, continuously variable transmission, in *2014 IEEE International Conference on Robotics and Automation* (ICRA, 2014), pp. 2913–2918.
17. G. A. Pratt, M. M. Williamson, Series elastic actuators, in *1995 IEEE/RSJ International Conference on Intelligent Robots and Systems 95. 'Human Robot Interaction and Cooperative Robots', Proceedings* (IEEE, 1995), vol. 1, pp. 399–406.
18. J. W. Sensinger, R. F. Weir, Design and analysis of a non-backdrivable series elastic actuator, in *9th International Conference on Rehabilitation Robotics, 2005* (ICORR, 2005), pp. 390–393.
19. R. R. Ma, L. U. Odhner, A. M. Dollar, A modular, open-source 3d printed underactuated hand, in *2013 IEEE International Conference on Robotics and Automation (ICRA)* (IEEE, 2013), pp. 2737–2743.
20. A. M. Dollar, R. D. Howe, The highly adaptive SDM hand: Design and performance evaluation. *Int. J. Rob. Res.* **29**, 585–597 (2010).
21. A. M. Dollar, R. D. Howe, The SDM hand as a prosthetic terminal device: A feasibility study, in *2007 IEEE 10th International Conference on Rehabilitation Robotics* (IEEE, 2007), pp. 978–983.
22. M. C. Carrozza, G. Cappiello, G. Stellin, F. Zaccone, F. Vecchi, S. Micera, P. Dario, A cosmetic prosthetic hand with tendon driven under-actuated mechanism and compliant joints: Ongoing research and preliminary results, in *Proceedings of the 2005 IEEE International Conference on IEEE Robotics and Automation* (ICRA, 2005), pp. 2661–2666.
23. S. A. Dalley, T. E. Wiste, T. J. Withrow, M. Goldfarb, Design of a multifunctional anthropomorphic prosthetic hand with extrinsic actuation. *IEEE ASME Trans. Mechatron.* **14**, 699–706 (2009).
24. M. Controzzi, C. Cipriani, B. Jehenne, M. Donati, M. C. Carrozza, Bio-inspired mechanical design of a tendon-driven dexterous prosthetic hand. *Conf. Proc. IEEE Eng. Med. Biol. Soc.* **2010**, 499–502 (2010).
25. B. Massa, S. Roccella, M. C. Carrozza, P. Dario, Design and development of an underactuated prosthetic hand, in *Proceedings of the 2002 IEEE International Conference on Robotics and Automation (2002)* (IEEE, 2002), vol. 4, pp. 3374–3379.
26. R. Ozawa, K. Hashirii, H. Kobayashi, Design and control of underactuated tendon-driven mechanisms, in *ICRA'09 Proceedings of the 2009 IEEE International Conference on Robotics and Automation* (IEEE Press, 2009), pp. 1522–1527.
27. C. Cipriani, M. Controzzi, M. C. Carrozza, The SmartHand transradial prosthesis. *J. Neuroeng. Rehabil.* **8**, 29 (2011).
28. M. G. Catalano, G. Grioli, E. Farnioli, A. Serio, C. Piazza, A. Bicchi, Adaptive synergies for the design and control of the Pisa/IIT SoftHand. *Int. J. Rob. Res.* **33**, 768–782 (2014).
29. L. U. Odhner, L. P. Jentoft, M. R. Claffee, N. Corson, Y. Tenzer, R. R. Ma, M. Buehler, R. Kohout, R. D. Howe, A. M. Dollar, A compliant, underactuated hand for robust manipulation. *Int. J. Rob. Res.* **33**, 736–752 (2014).
30. M. Manti, T. Hassan, G. Passetti, N. D'Elia, C. Laschi, M. Cianchetti, A bioinspired soft robotic gripper for adaptable and effective grasping. *Soft Robot.* **2**, 107–116 (2015).
31. J. R. Tumbleston, D. Shirvanyants, N. Ermoshkin, R. Janusziewicz, A. R. Johnson, D. Kelly, K. Chen, R. Pinschmidt, J. P. Rolland, A. Ermoshkin, E. T. Samulski, J. M. DeSimone, Continuous liquid interface production of 3D objects. *Science* **347**, 1349–1352 (2015).
32. B. Berman, 3-D printing: The new industrial revolution. *Bus. Horiz.* **55**, 155–162 (2012).
33. H. T. Hahn, E. A. Kempner, S. S. Lee, The stress development during filament winding of thick cylinders. *Composites Manufacturing* **4**, 147–156 (1993).
34. Elastomeric Polyurethane Carbon; www.carbon3d.com/materials/epu-elastomeric-polyurethane/.
35. J. T. Belter, J. L. Segil, A. M. Dollar, R. F. Weir, Mechanical design and performance specifications of anthropomorphic prosthetic hands: A review. *J. Rehabil. Res. Dev.* **50**, 599–618 (2013).
36. R. F. Weir, J. W. Sensinger, Design of artificial arms and hands for prosthetic applications, in *Standard Handbook of Biomedical Engineering and Design* (McGraw-Hill Professional, 2003), chap. 32.
37. R. Patel, R. E. Cox, N. Correll, Integrated force and distance sensing using elastomer-embedded commodity proximity sensors, Report No. SAND-2017-1719J. Sandia National Laboratory, Albuquerque, NM (2017).
38. J. Pratt, B. Krupp, C. Morse, Series elastic actuators for high fidelity force control. *Ind. Rob. Int. J.* **29**, 234–241 (2002).
39. A. H. Muhr, A. D. Roberts, Rubber abrasion and wear. *Wear* **158**, 213–228 (1992).
40. G. Walck, R. Haschke, M. Meier, H. Ritter, Robot self-protection by virtual actuator fatigue: Application to tendon-driven dexterous hands during grasping, in *Intelligent Robots and Systems (IROS), 2017 IEEE/RSJ International Conference on* (IEEE, 2017), pp. 2200–2205.
41. J. Morrow, S. Hemleben, Y. Menguc, Directly fabricating soft robotic actuators with an open-source 3-D printer. *IEEE Robot. Automation Lett.* **2**, 277–281 (2017).
42. T. J. Wallin, J. H. Pikul, S. Bodkhe, B. N. Peele, B. C. Mac Murray, D. Therriault, B. W. McEnerney, R. P. Dillon, E. P. Giannelis, R. F. Shepherd, Click chemistry stereolithography for soft robots that self-heal. *J. Mater. Chem. B* **5**, 6249–6255 (2017).
43. C. S. Haines, M. D. Lima, N. Li, G. M. Spinks, J. Foroughi, J. D. W. Madden, S. H. Kim, S. Fang, M. J. de Andrade, F. Goktepe, O. Goktepe, S. M. Mirvakili, S. Naficy, X. Lepro, J. Oh, M. E. Kozlov, S. J. Kim, X. Xu, B. J. Swedlove, G. G. Wallace, R. H. Baughman, Artificial muscles from fishing line and sewing thread. *Science* **343**, 868–872 (2014).
44. L. N. Awad, J. Bae, K. O'Donnell, S. M. M. De Rossi, K. Hendron, L. H. Sloot, P. Kudzia, S. Allen, K. G. Holt, T. D. Ellis, C. J. Walsh, A soft robotic exosuit improves walking in patients after stroke. *Sci. Transl. Med.* **9**, eaai9084 (2017).
45. Y. Ding, I. Galiana, A. T. Asbeck, S. M. M. De Rossi, J. Bae, T. R. T. Santos, V. L. de Araujo, S. Lee, K. G. Holt, C. Walsh, Biomechanical and physiological evaluation of multi-joint assistance with soft exosuits. *IEEE Trans. Neural Syst. Rehabil. Eng.* **25**, 119–130 (2017).
46. P. Polygerinos, Z. Wang, K. C. Galloway, R. J. Wood, C. J. Walsh, Soft robotic glove for combined assistance and at-home rehabilitation. *Robot. Autonomous Sys.* **73**, 135–143 (2015).
47. P. Polygerinos, S. Lyne, Z. Wang, L. F. Nicolini, B. Mosadegh, G. M. Whitesides, C. J. Walsh, Towards a soft pneumatic glove for hand rehabilitation, in *2013 IEEE/RSJ International Conference on Intelligent Robots and Systems (IROS)* (IEEE, 2013), pp. 1512–1517.
48. A. Arienti, M. Calisti, F. Giorgio-Serchi, C. Laschi, Poseidrone: Design of a soft-bodied ROV with crawling, swimming and manipulation ability, in *Oceans-San Diego* (IEEE, 2013), pp. 1–7.
49. H. G. Marques, M. Christophe, A. Lenz, K. Dalamagkidis, U. Culha, MYOROBOTICS: A modular toolkit for legged locomotion research using musculoskeletal designs, presented at the 6th International Symposium on Adaptive Motion of Animals and Machines, Darmstadt, Germany, 11 to 13 March 2013 (AMAM, 2013).
50. R. Pfeifer, P. Y. Tao, H. G. Marques, S. Weydert, D. Brum, M. Weyland, R. Hostettler, F. Volkert, V. Gmünder, D. Halbeisen, Roboy anthropomimetic robot (2013); https://roboy.org/.

Acknowledgments: We thank R. Weir and J. Segil for feedback and support during this project, the Cornell Center for Materials Research, and M. Silberstein. **Funding:** Research reported in this publication was supported, in part, by the National Center for Advancing Translational Sciences of the NIH under award number TL1TR002386. The content is solely the responsibility of the authors and does not necessarily represent the official views of the NIH. This research was also supported by the Air Force Office of Scientific Research under award number FA9550-18-1-0243 and the Office of Naval Research Young Investigator Award under award number N00014-17-1-2837. This work made use of the Cornell Center for Materials Research Shared Facilities, which are supported through the NSF MRSEC program (DMR-1719875). **Author contributions:** R.F.S. supervised the research, designed experiments, and edited the manuscript. K.W.O. conceived the EPT, designed and conducted experiments, and drafted the manuscript. A.X. designed and conducted experiments, data analysis, and theoretical modeling. D.J.L. created and assembled the ADEPT hand, designed and conducted experiments, and edited the manuscript. C.A.A., H.-J.Y., and M.F.X. conducted experiments and data analysis. L.W.W. assisted in the design of the ADEPT hand. **Competing interests:** K.W.O. and R.F.S. are listed as inventors on a U.S. provisional patent application (62/560,434) submitted by Cornell University that covers fundamental principles and designs of the EPT. The other authors declare that they have no competing financial interests. **Data and materials availability:** All data needed to evaluate the conclusions in this paper are present in the paper or the Supplementary Materials. Contact R.F.S. for materials.

Submitted 22 June 2018
Accepted 12 September 2018
Published 17 October 2018
10.1126/scirobotics.aau5543

Citation: K. W. O'Brien, A. Xu, D. J. Levine, C. A. Aubin, H.-J. Yang, M. F. Xiao, L. W. Wiesner, R. F. Shepherd, Elastomeric passive transmission for autonomous force-velocity adaptation applied to 3D-printed prosthetics. *Sci. Robot.* **3**, eaau5543 (2018).

Science Robotics

Elastomeric passive transmission for autonomous force-velocity adaptation applied to 3D-printed prosthetics

Kevin W. O'Brien, Artemis Xu, David J. Levine, Cameron A. Aubin, Ho-Jung Yang, Michael F. Xiao, Lennard W. Wiesner, and Robert F. Shepherd

Sci. Robot. **3** (23), eaau5543. DOI: 10.1126/scirobotics.aau5543

Science Robotics (ISSN 2470-9476) is published by the American Association for the Advancement of Science. 1200 New York Avenue NW, Washington, DC 20005. The title *Science Robotics* is a registered trademark of AAAS.